Building and Environment 252 (2024) 111273

Contents lists available at ScienceDirect

Building and Environment

journal homepage: www.elsevier.com/locate/buildenv

Partitioning mechanisms and film formations of DEHP on realistic indoor airborne particles and road dust

Zhuo Chen [b,c], Fanxuan Xia [b], Yujie Fan [b], Yi Jiang [c], Ying Xu [b], Jinhan Mo [a,b,d,e,f,*]

[a] College of Civil and Transportation Engineering, Shenzhen University, Shenzhen, 518060, China
[b] Beijing Key Laboratory of Indoor Air Quality Evaluation and Control, Department of Building Science, Tsinghua University, Beijing, 100084, China
[c] Department of Civil and Environmental Engineering, The Hong Kong Polytechnic University, Kowloon, Hong Kong, China
[d] Key Laboratory of Coastal Urban Resilient Infrastructures (Shenzhen University), Ministry of Education, Shenzhen, 518060, China
[e] Key Laboratory of Eco Planning & Green Building (Tsinghua University), Ministry of Education, Beijing, 100084, China
[f] State Key Laboratory of Subtropical Building and Urban Science, South China University of Technology, Guangzhou, 510641, China

ARTICLE INFO

Keywords:
Indoor air quality
Phthalate ester
Particle
Partition coefficient
Mechanistic model

ABSTRACT

In order to investigate the key factors resulting in the large deviations of the literature-reported PAE partition coefficients on particles, a direct particle sampling and DEHP partition coefficient-detecting method was developed to analyze realistic indoor airborne particles (AirP), Arizona test dust (ATD) and Beijing road dust (BJD). Mechanistic models were developed to determine the partition coefficients. Our results showed that the AirP partition coefficient (K_{ap}) of DEHP was 4.03×10^4 m^3/g, and the DEHP absorption in AirP organic matters dominates the sorption capacity. We found that the realistic AirP organic matter components varied from the traditional hypothesis that assumes organic matter is similar to octanol. In contrast, the DEHP partition coefficients (K_{dust}) for ATD and BJD were two orders of magnitude smaller than that of AirP. DEHP adsorption on the inorganic matter was found to be the main sorption mechanism on the surfaces of ATD and BJD. Following an 8-day DEHP exposure, the adhesion forces increased approximately from 4.0 nN to 11.0 nN for AirP and BJD, indicating the formation of organic films. These films could potentially enrich other organic pollutants to generate more hazardous combined pollution. This study provides a direct particle sorption method and more accurate partition coefficients to correctly evaluate DEHP concentrations in airborne particles and settled dust in indoor environments.

1. Introduction

Phthalate ester (PAE) is a type of semi-volatile organic compound (SVOC). Some toxic PAEs have posed a serious burden on human health [1]. The main pathways for human exposure to PAE include inhalation, ingestion, and dermal absorption [2–4]. Compared with volatile organic compounds (VOC) [5,6], PAE has a larger molecular weight and stronger adsorption, resulting in its continuous accumulation on airborne particles and settled dust [7]. Children tend to ingest large amounts of PAEs by inhaling airborne particles and ingesting settled dust [8]. In order to evaluate human exposure to particle- and dust-phase PAEs, Weschler and Nazaroff [9,10] provided ground-breaking fundamental mechanisms to describe the gas-particle interactions of PAE. Their theoretical framework made the indoor PAE transporting process clearer and was widely applied in the following modelling and experimental studies [11–14]. Nevertheless, there are still some research gaps in the current methods for describing the partitioning behaviors of PAEs on particles, which may introduce errors in calculating PAE partition coefficients [15]. For instance, PAEs are assumed mainly enriched in the organic films on particle surfaces, the component and fraction of which are assumed constant. The assumptions lead to relatively large deviations in evaluating human PAE uptake. Thus, we endeavor to close the research gaps by designing and conducting experiments to quantify the PAE sorption capacity and states on particles.

Compared with the PAE sorption studies on indoor surfaces [16–19], it is relatively difficult to conduct sorption experiments on airborne particles and settled dust mainly due to the small particle size. The sizes of airborne particles are generally no more than 10 μm, most of which are between 0 and 2.5 μm [20,21]. The settled dust is nearly 2–3 orders of magnitude larger than airborne particles in diameter [10]. Thus,

* Corresponding author. College of Civil and Transportation Engineering, Shenzhen University, Shenzhen, 518060, China.
E-mail address: mojinhan@szu.edu.cn (J. Mo).

https://doi.org/10.1016/j.buildenv.2024.111273
Received 9 July 2023; Received in revised form 6 January 2024; Accepted 3 February 2024
Available online 5 February 2024

researchers find it difficult to collect particles quantitatively. Meanwhile, chamber sorption experiments are also hard to apply for particles considering their deposition and resuspension characteristics in a restricted environment [11].

For airborne particles, researchers applied two methods to determine the PAE partition coefficients: field test and simulated particle generation. There are many field-test studies to explore the PAE concentrations in gas and airborne particles in residences [22–25], offices [26], hospitals [27] and traffic micro-environments [28]. However, due to the lack of mass concentrations of airborne particles, the PAE partition coefficients of airborne particles could not be calculated generally. Wang et al. separately analyzed the PAE (both in gas and particle phase) and airborne-particle concentrations through field tests in residences by field test, and calculated the PAE partition coefficients of airborne particles based on the results [7]. The field-test method has a potential problem in guaranteeing whether the PAEs have reached the gas and particle phase sorption equilibrium. While others characterized the PAE partition coefficients using artificial airborne particles. They generated the simulated particles with the textures of inorganic salt [29], organic matter [30], or combustion products [31]. The particles were then introduced into PAE exposure chambers for sorption experiments. Nevertheless, there are significant differences in composition between the simulated particles and the realistic indoor airborne particles.

Settled dust is relatively easier to collect compared to airborne particles. However, the sorption-experiment conducting and PAE concentration analysis on dust are also challenging. Bi et al. characterized the dust partition coefficients of butyl benzyl phthalate (BBP) and di (2-ethyl-hexyl) phthalate (DEHP) by field test [12]. Then, they directly collected indoor settled dust from a vacuum bag and sprayed it over the surfaces of PAE source materials for sorption experiments in a subsequent study [13]. A similar method was also reported in Li et al.'s study [32]. However, the inadequate contact between settled dust and source material would introduce errors in concentration analysis during the dust sorption experiment.

Meanwhile, the PAE partitioning performances on particulate matters, including airborne particles and settled dust, are significantly affected by particle characteristics [7,29,30] and environmental factors like humidity [13] and temperature [31,33]. Wu et al. [30] measured the DEHP partition coefficients of inorganic and organic artificial particles in a specially designed tube chamber. They found that the partition coefficients varied largely between different particles. Zhou et al. [31] conducted sufficient research on the effects of temperature and humidity on partitioning behaviors between gas- and particle-phase PAEs. They found that temperature has a strong negative impact on the PAE partition coefficients, and humidity had a smaller effect than temperature. Thus, it is crucial to apply realistic particulate matter and control environmental factors during the sorption experiments for a more accurate PAE-partition-coefficient determination. We then developed a chamber-based method applying fibrous glass membranes to quantitatively hold the realistic particles, and also mimic the real indoor environmental factors. To the best of our knowledge, there is no further study applying fibrous glass membranes as basements to determine the PAE sorption capacities of airborne particles and settled dust. The reason may be that researchers found it hard to decouple the PAE amounts in particles from membrane samples since PAE could adsorb in both particles and glass membranes during the sorption experiments. Therefore, we further developed mechanistic models to decouple the PAE sorption amounts in particles during the mass transfer process. The PAE partition coefficients of airborne particles and settled dust can then be obtained by model fittings on the experimental data.

In this study, we applied the glass-membrane-based method combined with the chamber sorption experiments to characterize the PAE sorption behaviors on realistic indoor airborne particles by sampling them from indoor air. As for the settled dust, it is hard to collect the realistic indoor settled dust because of other impurities (like hair, food debris, etc.) existing on indoor floorings. Thus, we applied the Arizona test and Beijing road dust as substitutes for the indoor settled dust. DEHP was chosen as the target PAE. The aims of this research include: (1) developing a direct particle sampling and DEHP partition coefficient-detecting method based on the fibrous glass membrane; (2) experimentally determining the partition coefficients of the realistic indoor airborne particles and road dust, decoupling the sorption capacities of DEHP by the organic and inorganic components in particles; (3) observing the sorption states of DEHP on particles in a microscopic view, and studying the organic film formation mechanisms on airborne particles and road dust.

2. Materials and methods

2.1. Source material and glass membrane

A wallpaper sample acquired from an online store (YUZHIFANG Inc.) was used as the DEHP source material in this study, the thickness of which is 1 mm. The gaseous DEHP concentration immediately adjacent to the source material (y_0, μg/m^3) was experimentally detected in this study. The value is determined as 2.08 ± 0.38 μg/m^3, and details of the test method can be seen in *Section S1* of the Supplementary Material. As revealed by Xu's study [34], the parameter y_0 and material-phase DEHP concentration (C_0, %) were constants for several years.

The experiments used fibrous glass membranes to load airborne particles and dust, considering the good particle-capture performance and heat stability. The membranes were purchased from Qinghuan Technologies Inc (Shenzhen, China), composed of glass fibers (~1 μm in diameter) with 47 mm in diameter and 0.4 mm in thickness. The mass, surface morphology and true density of the membrane were characterized by the microbalance (ME 104E, Mettler Toledo, Switzerland), scanning electron microscope (Merlin, Carl Zeiss AG, Germany) and true density analyzer (AccuPyc II 1340, Micromeritics Inc., USA), respectively (see *Section S2* of the Supplementary Material for details). Based on the obtained membrane mass (m_{mem}, g) and true density (ρ_{true}, g/m^3), the porosity of the glass membrane (ε_{mem}) can then be calculated by eq. (1).

$$\varepsilon_{mem} = \frac{\pi(d_{mem}/2)^2\delta_{mem} - m_{mem}/\rho_{true}}{\pi(d_{mem}/2)^2\delta_{mem}} \quad (1)$$

where d_{mem} and δ_{mem} are the diameter and thickness of the glass membrane, respectively, m.

2.2. Sample preparation and characterization

The realistic airborne particles were directly loaded on the blank fibrous glass membranes in the indoor environment. The airborne particles were named AirP, while the membrane-contained airborne particles were named M-AP. A sampler was designed to prepare the M-AP samples. As shown in Fig. 1a, the sampler comprises two cylindrical stainless steel tubes, 38 mm in diameter and 50 mm in length. The left tube was welded with a cone tube, while the right one had a short stainless steel tube (6 mm in diameter) connected to the side of the cylinder for air sampling. A glass membrane with a seal ring could be placed between the two tubes, and then sealed by lathedog. We set the sampler in a room with windows open in Beijing, China, and connected it with a sampling pump (LINEAIR 40, BUCK Inc., USA) through the short tube (seen in Fig. 1a). The sampling airflow, Q_{samp}, and time were controlled at 10 L/min and 12 h, respectively.

Arizona test dust (ATD) and Beijing road dust (BJD) were chosen to prepare dust samples. The ATD, the road dust in Arizona (USA), was purchased from Powder Technology Inc., ranging from 1 μm to 10 μm in diameter. BJD was collected inside the campus of Tsinghua University and then sieved to less than 75 μm. The specific surface areas of ATD and BJD were characterized by the Brunauer-Emmett-Teller (BET) specific

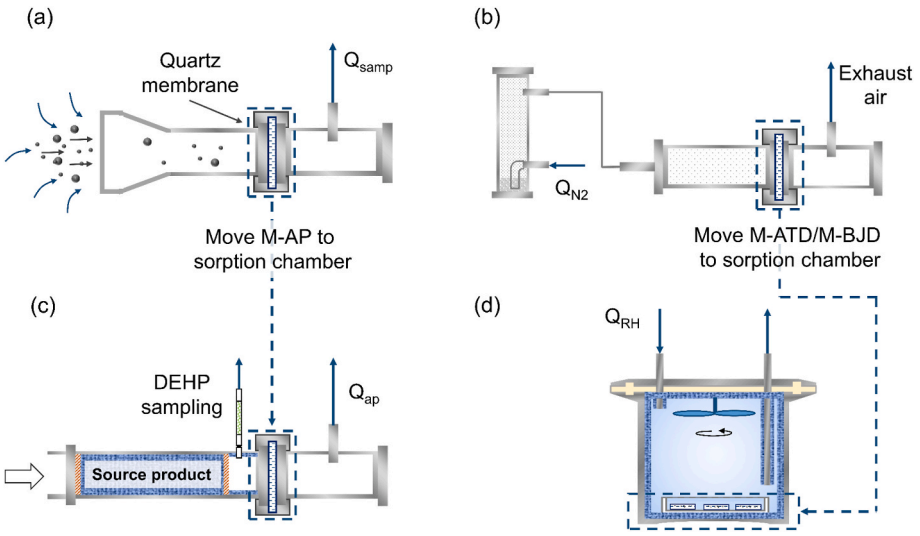

Fig. 1. Schematics of (a) airborne particle sampler, (b) dust sampler, (c) the tube-like M-AP sorption chamber and (d) the jar-like M-ATD or M-BJD sorption chamber.

area analyzer (IQ2, Quantachrome Instruments, USA). The elemental compositions of ATD and BJD were also analyzed by inductively coupled plasma mass spectrometry (8800, Agilent Technologies, USA). Especially the oxidation states and contents of the iron element in ATD and BJD were characterized by X-ray Photoelectron Spectroscopy (ESCALAB 250XI, Thermo Fisher Scientific, USA). Another sampler was designed to load dust on blank membranes, as shown in Fig. 1b. The dust sampler was similar to that for airborne particles. The difference lies in the left tube of the dust sampler connecting with an air duct instead of welding a cone tube. We designed a dust container with two stainless steel tubes symmetrically welded on the body. The target dust was heaped up to nearly 50 mm in depth in the dust container. The top tube was connected with the air duct of the dust sampler by a hose and Teflon tube. We introduced a nitrogen airflow, Q_{N2} (4 L/min), through the bottom tube into the dust container to sweep the dust. Then, the airflow carried dust together to go through air ducts and reach the glass membrane in the dust sampler. We then obtained the membranes loaded with ATD and BJD, named M-ATD and M-BJD, respectively.

After finishing the sample preparation, we characterized the physical properties of M-AP, M-ATD and M-BJD, including mass, surface morphology and true density. As mentioned above, the test methods were the same as those on blank glass membranes. Meanwhile, the organic carbon amounts contained in the samples were also determined by a thermal/optical carbon analyzer (TOC-L, SHIMADZU, Japan). The instrument and method were widely used to analyze the particle organic/inorganic ratio [13]. Details about the test methods and parameters can be seen in *Section S2* of the Supplementary Material.

2.3. Sorption experiments

Two sorption chambers, including the tube-like chamber (Fig. 1c) and the jar-like chamber (Fig. 1d), were designed for the membrane samples to mimic the DEHP adsorption processes on airborne particles (AirP) and settled dust (ATD and BJD) in the realistic indoor environment, respectively. Both chambers were placed in an incubator to control the temperature constantly at 25.0 ± 0.5 °C.

After the M-AP sample was prepared and weighed, the prepared M-AP in Fig. 1a was installed and sealed in the membrane holder (6.5 mm in diameter) in the tube-like chamber, as shown in Fig. 1c. Wallpaper pieces (10 × 10 mm^2) as DEHP sources were loaded on the inner surfaces of a 180 mm tube at the upstream of the holder. Two metal nets were fastened at both sides of the wallpaper pieces for fixation. Then, an air compressor (750W, Fujiwara, Japan) provided clean airflow, Q_{ap}, through the wallpaper pieces at 40 L/min (2.4 m^3/h). Gaseous DEHP released from the wallpaper pieces will be adsorbed by the particles and glass fibers in the M-AP sample at a face velocity of 0.59 m/s. The face air velocity of the M-AP sample inside the tube-like chamber was calculated by combining the airflow rate, Q_{ap}, provided by the air compressor and the sectional area of the tube-like chamber. Details about the calculation process were specified in *Section S3* of the Supplementary Material. Since both the airflow rate and tube sectional area were held consistently, the face velocities inside the tube-like chamber could then be guaranteed as stable for all cases of sorption experiments. The sorption experiments were conducted to simulate the DEHP sorption process on airborne particles in indoor environments because of their similar mass convection coefficients (details can be seen in *Section 3.2*). The exposed M-AP sample was then taken out and prepared as strips, the procedures of which were described in detail in *Section S3* of the Supplementary Material. The strips were inserted into empty thermal desorption cartridges for DEHP concentration analysis. We applied five strips of each exposed M-AP sample as parallels to analyze the DEHP concentrations.

The jar-like chamber for M-ATD or M-BJD has been used for sorption experiments on indoor substrates [18] and organic films [19]. The chamber was designed as a cylinder with DEHP source products pasted on inner surfaces. Two tubes that differed in length were welded symmetrically on the lid. A fan was designed to fix the lid and enhance the mass transfer inside the chamber. Details about the chamber size can be seen in our previous research [18]. After the M-ATD or M-BJD sample was prepared and weighed, the sample was cut into strips and transferred into a 90 mm-diameter glass petri dish in order by a clean tweezer. The glass petri dish was then set on the bottom of the jar-like chamber. After sealing the chamber, the fan was turned on. Then an airflow of 1 L/min, Q_{RH}, with a relative humidity of 50% was introduced to the chamber. After specific time exposure, three strips were moved from the chamber into empty thermal desorption cartridges for DEHP concentration analysis. Details about the cartridge sample concentration analysis by thermal desorption method and QA/QC analysis of the method can be seen in *Section S4* of the Supplementary Material.

2.4. Mechanistic models

DEHP mass transfer processes from air to AirP and ATD/BJD on the membrane samples are schematically shown in Fig. 2a and b.

Airflow passed by the DEHP source fillers in the tube-like chamber and carried gaseous DEHP from source materials to the M-AP sample through convection. We applied a high airflow rate in the tube-like chamber to provide a large mass transfer coefficient to the M-AP sam-

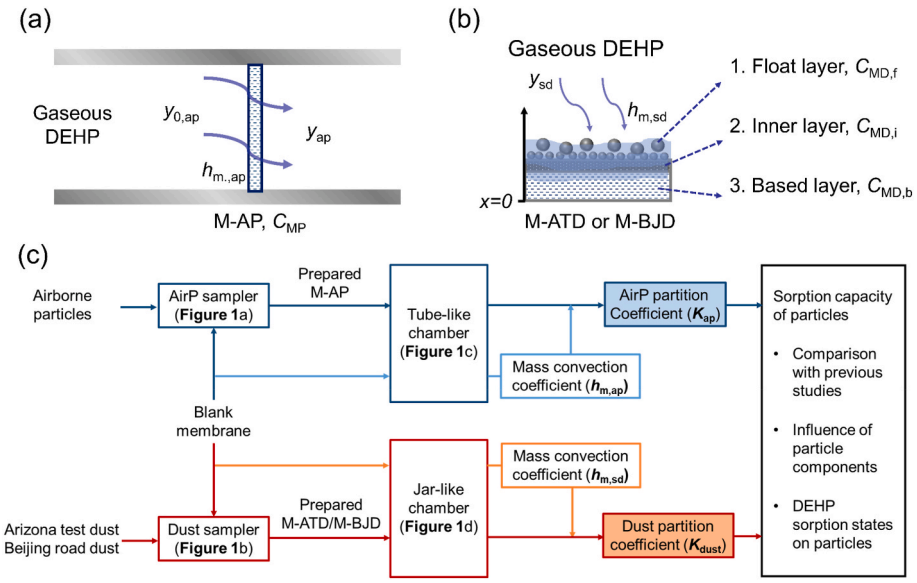

Fig. 2. Mass transfer processes of DEHP on samples in (a) the tube-like chamber for M-AP sorption and (b) the jar-like chamber for M-ATD or M-BJD sorption, and (c) a modular framework for sorption-experiment conducting to characterize the mass convection coefficients ($h_{m,ap}$ and $h_{m,sd}$) and partition coefficients (K_{ap} and K_{dust}).

ple, which can then mimic the DEHP sorption process on airborne particles in real indoor environments. Since the airflow rate was quite large in the tube-like chamber, we applied a lumped-parameter model to the M-AP sample, in which the mass transfer coefficient was applied to normalize the face velocity in the chamber. Meanwhile, the gaseous DEHP concentrations adjacent to the membrane and particles in the M-AP sample were assumed as the same, which has been frequently used in the relevant modeling research [35]. According to Table S2 of the Supplementary Material, the particle's volume fraction was much smaller than the whole M-AP sample. Thus, it was assumed that both blank glass membranes and M-AP samples have the same porosity and physical structure. The DEHP mass transfer process in the tube-like chamber could be described by the governing equations as shown in eqs. (2)–(4).

$$\varepsilon_{mem} V_{mem} \frac{dy_{ap}}{dt} + V_{mem} \frac{dC_{MP}}{dt} = Q_{ap}\left(y_{0,ap} - y_{ap}\right) \tag{2}$$

$$V_{mem} \frac{dC_{MP}}{dt} = h_{m,ap} A_{in,MP}\left(y_{ap} - y_{MP}\right) \tag{3}$$

$$C_{MP} = \left(K_{mem} + M_{ap} K_{ap}\right) y_{MP} \tag{4}$$

where V_{mem} is the volume of the membrane, m^3; y_{ap} is the gaseous DEHP concentration in the membrane interspace and outlet of chamber, μg/m^3; C_{MP} stands for the solid-phase DEHP concentration of M-AP samples, μg/m^3; Q_{ap} is the airflow rate in the tube-like chamber, m^3/h; $y_{0,ap}$ is the gaseous DEHP concentration of the airflow in front of the M-AP sample, μg/m^3, the value of which was the same as y_0 according to Fig. S1 of the Supplementary Material; $h_{m,ap}$ is the mass convection coefficient, m/h; $A_{in,MP}$ is the inner surfaces of the M-AP sample, m^2; y_{MP} is the gaseous DEHP concentration near the surfaces of the solid-material M-AP sample, μg/m^3; K_{mem} stands for the DEHP partition coefficient of blank glass membrane, dimensionless; M_{ap} is the particle mass concentration in the M-AP sample, μg/m^3. K_{ap} is the DEHP partition coefficient of airborne particles, m^3/μg. The parameters of M-AP physical structure, flow field and solid-phase concentration can be obtained with the knowledge of sample measurement and sorption experiments. The parameter K_{ap} can be derived through model fitting on C_{MP} variation over time. The values of M_{ap} and $A_{in,MP}$ can be seen in Table S2 and Table S3 of the Supplementary Material.

In the jar-like chamber for dust sorption, gaseous DEHP was emitted from the source products and adsorbed on the sink materials, including glass petri dish and M-ATD or M-BJD samples. Considering the air disturbance by the fan and ventilation, the air was assumed to be uniformly mixed in the chamber. Thus, the DEHP mass transfer process in the air can be described as eq. (5).

$$V_{cham} \frac{dy_{sd}}{dt} = -y_{sd} Q_{RH} + h_{m,sd} A_{source}\left(y_0 - y_{sd}\right) + h_{m,sd} A_{dish}\left(y_{dish} - y_{sd}\right) + h_{m,sd} A_{mem}\left(y_{MD,f} - y_{sd}\right) \tag{5}$$

where V_{cham} means the volume of the jar-like chamber, m^3; y_{sd} is the gaseous DEHP concentration in the chamber, μg/m^3; Q_{RH} is the ventilation rate, m^3/h; $h_{m,sd}$ is the mass convection coefficients on inner chamber surfaces, m/h; A_{source} and A_{dish} are the surface areas of source materials in chamber, and petri dish, respectively, m^2; y_{dish} and $y_{MD,f}$ are the gaseous DEHP concentration adjacent to the surfaces of the petri dish and dust samples, respectively, μg/m^3. DEHP sorption amounts on petri dishes can be determined by the mass flux transferred through the boundary layer, as shown in eq. (6).

$$K_{dish} \frac{dy_{dish}}{dt} = h_{m,sd}\left(y_{sd} - y_{dish}\right) \tag{6}$$

where K_{dish} is the DEHP partition coefficient on the glass substrate, m, the value of which is 700 m according to our previous study [18]. The DEHP sorption on the M-ATD or M-BJD sample was relatively complex, considering its porous structure. According to the surface morphologies of M-ATD and M-BJD in Fig. S2, dust filled the surface pores and stacked them on the surface of the glass membrane. Thus, gaseous DEHP tended to infiltrate the sample through the air gaps between dust and glass fibers in the membrane and then partitioned on the solid phase. We modeled the dust sample as three layers in spatial structure and named them as float layer, inner layer and based layer, respectively, as shown in Fig. 2b. The governing equation describing the DEHP diffusion and sorption with the three sample layers can be seen as eqs. (7)–(9):

$$\delta_f \varepsilon_f \frac{dy_{MD,f}}{dt} + \delta_f\left(1 - \varepsilon_f\right) \frac{dC_{MD,f}}{dt} = h_{m,sd}\left(y_{sd} - y_{MD,f}\right) + D_{a,f,i} \frac{y_{MD,i} - y_{MD,f}}{\left(\delta_f + \delta_i\right)/2} \tag{7}$$

$$\delta_i \varepsilon_i \frac{dy_{MD,i}}{dt} + \delta_i\left(1 - \varepsilon_i\right) \frac{dC_{MD,i}}{dt} = D_{a,f,i} \frac{y_{MD,f} - y_{MD,i}}{\left(\delta_f + \delta_i\right)/2} - D_{a,b} \left.\frac{\partial y_{MD,b}}{\partial x}\right|_{x=\delta_b} \tag{8}$$

$$\varepsilon_{mem}\frac{\partial y_{MD,b}}{\partial t}+(1-\varepsilon_{mem})\frac{\partial C_{MD,b}}{\partial t}=D_{a,b}\frac{\partial^2 y_{MD,b}}{\partial x^2},\ \text{for } 0<x<\delta_b \quad (9)$$

where the footnotes, f, i and b, stand for the float layer, inner layer and based layer of the M-ATD or M-BJD sample, respectively; δ means the thickness of the target layer, m; ε is the porosity; y_{MD} and C_{MD} are the gas-phase and solid-phase DEHP in the sample, μg/m^3; $D_{a,f,i}$ is the DEHP diffusion coefficient between float layer and inner layer, while $D_{a,b}$ is the one in the based layer, m^2/h. It should be noted that the thicknesses of the float layer and inner layer are far smaller than that of the based layer, according to *Section S5* and Table S3 of the Supplementary Material. Thus, we applied the lumped parameter method on both the float and inner layers.

The parameters, y_{MD} and C_{MD}, are governed by partition coefficients of dust (K_{dust}, μg/g) and membrane (K_{mem}). According to the physical structure of each layer, the relationships between y_{MD} and C_{MD} can be described as eqs. (10-12):

$$C_{MD,f}=K_{dust}\rho_{dust}y_{MD,f} \quad (10)$$

$$C_{MD,i}=[(1-\varepsilon_i)K_{mem}+(\varepsilon_b-\varepsilon_i)\rho_{dust}K_{dust}]y_{MD,i} \quad (11)$$

$$C_{MD,b}=K_{mem}y_{MD,b} \quad (12)$$

The mass diffusion of DEHP only occurred in voids between dust and glass fibers in the sample as a porous media [13,36]. Thus, the diffusion coefficients, $D_{a,f,i}$ and $D_{a,b}$, can be calculated based on eqs. (13) and (14).

$$D_{a,f,i}=\frac{\delta_f+\delta_i}{\frac{\delta_f}{\varepsilon_f D_a}+\frac{\delta_i}{\varepsilon_i D_a}} \quad (13)$$

$$D_{a,b}=\varepsilon_{mem}D_a \quad (14)$$

The values of the parameters can be obtained from literature and direct measurements for both M-AP and M-ATD (or M-BJD) sorption models, as summarized in Table S3 of the Supplementary Material. It should be noted that the DEHP partition coefficient of the blank fibrous glass membrane (K_{mem}) is a key parameter coupling with K_{ap} and K_{dust} in M-AP, M-ATD and M-BJD samples. A preliminary experiment was designed to determine the parameter K_{mem} of DEHP, which can be seen in *Section S6* of the Supplementary Material. With the knowledge of K_{mem}, the partition coefficient, K_{ap} or K_{dust}, can be characterized using the sorption models following the modular framework shown in Fig. 2c. In brief, we first applied blank membranes on tube-like and jar-like chambers to conduct DEHP sorption experiments and obtain the mass convection coefficients, $h_{m,ap}$ and $h_{m,sd}$, respectively. Then, the DEHP sorption experiments were conducted on M-AP, M-ATD and M-BJD to characterize the particle partition coefficients by model fitting with the knowledge of mass convection coefficients.

3. Results

3.1. Partition coefficient of blank membrane

Fig. 3a shows the variation of solid-phase DEHP concentrations in blank membranes (C_{mem}) over time, obtained by a preliminary experiment shown in *Section S6* of the Supplementary Material. The C_{mem} rose rapidly during the initial 4-day exposure and reached stable after 19 days. Since the partition coefficient of the blank membrane (K_{mem}) was the only unknown parameter in the mass transfer model described as eqs. (S5-8) in *Section S6*, the experimental data was fitted in Fig. 3a to obtain K_{mem} as 1.86×10^8 ($R^2=0.9508$). According to the fitting curve, the membrane reached sorption balance approximately after a 10-day exposure. Thus, the method can determine the DEHP partition coefficients of porous materials more quickly and efficiently compared to previous researches [37].

3.2. DEHP partitioning on realistic airborne particles

According to the analysis of DEHP sorption processes in the M-AP samples, the mass convection coefficient, $h_{m,ap}$, was coupled with the partition coefficient of airborne particles, K_{ap}, in the mechanistic model

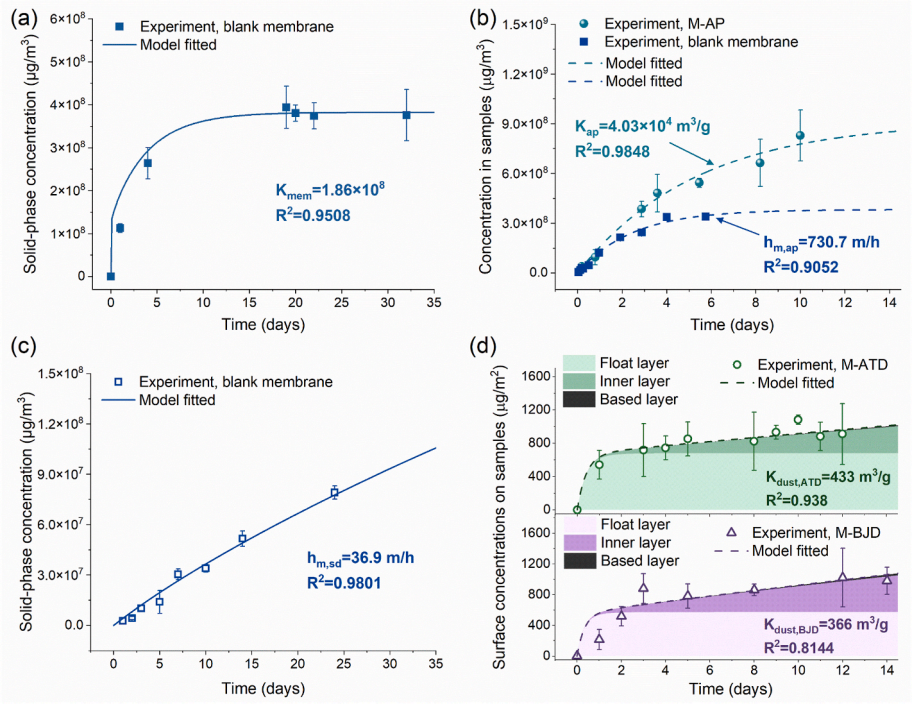

Fig. 3. (a) The variation of C_{mem} over time in the tube-like chamber to determine K_{mem}. (b) The solid-phase DEHP concentrations in blank membrane and M-AP samples in the tube-like chamber. (c) Experimental results of C_{mem} over time in the jar-like chamber to determine $h_{m,sd}$. (d) The solid-phase DEHP concentrations in M-ATD and M-BJD samples in the jar-like chamber. We applied five duplicated samples for (a) and (b), and three duplicated samples for (c) and (d) to obtain the means and standard deviations for each point in the figures.

described by eqs. (2)–(4). Thus, we first applied blank membranes in the tube-like chamber for M-AP samples to conduct the sorption experiment and determine the $h_{m,ap}$ under the 40 L/min-airflow rate. Herein, eq. (4) can then be transferred as eq. (15) for blank membranes in the tube-like chamber.

$$C_{MP} = K_{mem} y_{MP} \quad (15)$$

The exposure times were controlled from 1 to 138 h for blank membranes in the tube-like chamber. The blue points in Fig. 3b show the solid-phase DEHP concentrations in the blank membrane samples. The blank membrane reached sorption balance in the chamber approximately after 100-h mass convection. We applied the mass transfer model containing eqs. (2), (3) and (15) to fit the data and obtain $h_{m,ap}$ as 730.7 m/h ($R^2 = 0.9052$). The obtained $h_{m,ap}$ in this study is approaching the reported h_m of airborne particles in indoor environments, the values of which ranged from 7.82×10^2 to 1.19×10^4 m/h [35,38]. Thus, M-AP sorption experiments in the tube-like chamber can simulate well for the DEHP sorption on airborne particles in the indoor environment.

Applying the airborne particle sampler shown in Fig. 1a, we obtained a serial of M-AP samples loading airborne particles with 2.55 ± 0.8 g/m^2 in mass. The samples were conducted DEHP mass convection experiments in a tube-like chamber exposing 4.5–240 h. The mass transfer model described by eqs. (2)–(4) were applied on the experimental data to fit the K_{ap} of airborne particles, as shown in Fig. 3b, which was 4.03×10^4 m^3/g with an R^2 value of 0.9848. The experimental data were well fitted by the model, indicating the rationality of the model. The results revealed that the M-AP samples could not reach DEHP sorption balance after nearly a 240-h continuous exposure. It means the M-AP sample had a larger partition coefficient than the blank membrane after loading the airborne particles. Through the quantitative experiments and modeling analysis, we directly measured the K_{ap} of the realistic airborne particles in indoor environments.

3.3. DEHP partitioning on road dust

Similar as the tube-like chamber, we first applied sorption experiments on the blank membrane strips in the jar-like chamber to determine the mass convection coefficient, $h_{m,sd}$. The sorption experiments lasted 24 days, and the blank strip samples were taken out from the chamber to conduct a DEHP concentration analysis. Eqs. (5), (6) and (9) were used to fit the $h_{m,sd}$ as 36.9 m/h ($R^2 = 0.9801$), as shown in Fig. 3c. The experimental data and model curve grew near-linearly, meaning the blank membranes were far from sorption equilibrium during the 24 days' exposure in the chamber.

With the knowledge of $h_{m,sd}$, we placed M-ATD or M-BJD strip samples in the jar-like chamber to conduct DEHP sorption experiments. The exposure times were controlled for no more than 14 days for all samples. The surface DEHP concentrations of the samples were tested and shown in Fig. 3d. The surface DEHP concentrations increased significantly in the first one or two days and then enlarged slightly over time latterly. Applying the developed three-layer mechanistic model described by eqs. (7)–(9), we then fitted the K_{dust} as 433 m^3/g ($R^2 = 0.9380$) and 366 m^3/g ($R^2 = 0.8144$) for ATD and BJD, respectively. The surface DEHP concentrations in each layer of samples can also be obtained through the model analysis, as shown in Fig. 3d. After a 14-day exposure, the DEHP were mainly enriched in the float and inner layers, while the DEHP concentration ratios were no more than 2.5% in the based layers for both M-ATD and M-BJD samples. Details about the DEHP sorption kinetics from air to M-ATD and M-BJD samples were described in Section S7 of the Supplementary Material.

3.4. Comparison between K_{ap} and K_{dust}

Based on the model-fitted results, the K_{ap} parameter was approximately two orders of magnitude larger than K_{dust} values. As mentioned in Table S2 of the Supplementary Material, the organic carbon proportions were experimentally detected as 33.0%, 0.82% and 0.51%, respectively, for AirP, ATD and BJD. It means the AirP comprises significant amounts of organic matter, which were found covered on impermeable cores of airborne particles in a previous study [39]. While the ATD and BJD could be approximated as inorganic particles. Thus, the DEHP partitioning behavior on AirP may be discrepant with the two types of dust: DEHP could absorb in the organic matters of AirP and adsorb on the surface of inorganic road dust. The organic matter on AirP showed much larger sorption capacities than inorganic surfaces. The discovery of this study could support the assumption in Pankow's research [40]: indoor organic pollutants tend to be fully sorbed in organic matter and not to adsorb on inorganic surfaces of the indoor particles, which was widely applied in the studies latterly [2,3,41–43].

4. Discussion

4.1. Influencing factors on K_{ap}

Lots of researchers have been devoted to the K_{ap} determination. However, there are large deviations in K_{ap} values between different studies. Fig. 4a summarizes the reported K_{ap} values. The source of each reference is numbered in the figure, and details are listed in Table S4 of the Supplementary Material. The K_{ap} data were obtained from model estimation (red points in Fig. 4a) and experimental detection (green points in Fig. 4a), respectively.

There is a large deviation (more than three orders of magnitude) in the model-estimated K_{ap}, the values ranging from 4.8×10^3 to 9.4×10^6 m^3/g, except for the extreme data. Wei et al. have made an exhaustive summary of the empirical formulas of K_{ap} estimation [15]. The studies revealed empirical formulas as a log-linear relationship between K_{ap} and the physical properties of certain SVOCs, such as the vapor pressure (V_p) and octanol-air partition coefficient (K_{oa}). The target SVOCs used for empirical-formula developing contained PAHs (polycyclic aromatic hydrocarbons), PCBs (polychlorinated biphenyls) and organochlorine pesticides, but no PAEs remarkably. Since the molecular structures of PAEs and other SVOCs are quite different, it will introduce large errors in the K_{ap} estimation for PAEs applying these empirical formulas. It should be noted that Li et al. developed a fundamental model named the steady-state Li-Ma-Yang P/G equation, which can well describe the gas/particle partitioning behaviors of SVOCs [44]. Based on the Li-Ma-Yang P/G equation, they further raised the steady-state-based model of airborne particle/gas partitioning for SVOCs [45]. The theoretical prediction of K_{ap} was obtained as 2.90×10^4 m^3/g for DEHP from their model (see the red point of the 24th reference in Fig. 4a), the value of which indicates a nice matching with the experimental result of this study (4.03×10^4 m^3/g) compared to the three orders of magnitude deviations in literature. The other widely used model assumes the organic matter in particles is similar to octanol in affinity [9]. The assumption well simplified the tedious calculation process of K_{ap} from empirical formulas, and was widely applied in the following studies [11,35,39,42]. Nevertheless, there is a research gap that remains to be verified whether the organic matter is similar to octanol in physical property.

The experimentally determined K_{ap} showed nearly one order of magnitude deviations, the values of which ranged from 1.1×10^4 to 2.3×10^5 m^3/g. In the previous experimental studies, the airborne particles were artificially obtained in controllable ways. We detailed the target particle compositions in Fig. 4b. The particles composed of organic matters (oleic acid and squalane) [30] or a large part of organic matters (incense coil) [31] were measured to have large K_{ap} values. In contrast, the K_{ap} values of inorganic particles (ammonium sulfate, $(NH_4)_2SO_4$) were relatively smaller [29,30]. In this study, we directly applied DEHP sorption on the realistic indoor airborne particles, the K_{ap} value of which was between those of organic and inorganic particles. Wang et al. obtained the K_{ap} of DEHP by field tests in offices and residential buildings in Xi'an, China [7]. The K_{ap} value was tested nearly as 2.5×10^4 m^3/g,

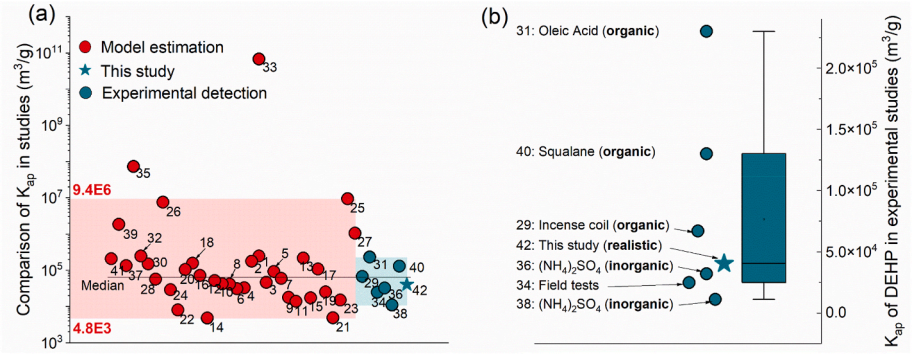

Fig. 4. (a) The reported K_{ap} of DEHP in literature obtained from model estimation and experimental detection. (b) The compositions of the particles used in the experimental studies. The reference numbers in figures correspond with those listed in Table S4.

similar to but slightly smaller than that of this study. It is probably because of the difference between the airborne particles in Beijing and Xi'an.

Considering the significant influence of particle organic compositions on the DEHP partition behaviors, we further detected species and contents of organic matter in the realistic airborne particles through thermal desorption. The tendency of organic-matter signals varies over molecular weight (MW), as shown in Fig. 5a. The organic-matter MWs ranged between 100 and 700, the median of which was 382. There is a variation between octanol and the organic matter in airborne particles in the property of molecular weight. However, it still remains to be explored whether there are significant differences between octanol and particle organic matter in other physicochemical properties, especially in SVOC partition coefficients. Weschler and Nazaroff [10] found a log-linear relationship between K_{oa} and SVOC partition coefficients. Thus, it is expected to develop a more accurate model to predict SVOC partition coefficients in realistic indoor organic films based on K_{oa} parameters, which is well worth studying in the future. Fig. 5b qualitatively analyzed the components of the organic matter. Their chemistry formulas can be summarized as $C_xH_yO_z$, $C_xH_yO_zSi_i$, $C_xH_yN_z(O_i)$, C_xH_y and others, the content proportions of which were 38.4%, 36.3%, 5.2%, 19.5% and 0.5%, respectively. Generally, $C_xH_yO_zSi_i$ stands for siloxane. In comparison, the others were more complex in molecular structures. Based on the mass spectrogram database supplied by Shimadzu Corporation, Fig. 5c summarizes the classes of organic matter. $C_xH_yO_z$ is composed of aldehyde, alcohol, carboxylic acid, ester and ether, in which the ester occupied the largest proportion (87.6%) among all the matters. Amine (77.0%) and Nitrile (23.0%) consisted of $C_xH_yN_z(O_i)$. And there is alkane (85.7%), PAH (2.0%) and olefin (12.3%) that comprise C_xH_y, where the PAH is detected as pyrene. Thus, the organic matters in realistic airborne particles were abundant in composition.

4.2. *Influence of inorganic matters on K_{dust}*

As the inorganic particles, the ATD and BJD enriched DEHP by surface adsorption. The K_{dust} values are 433 m^3/g and 366 m^3/g for ATD and BJD, respectively, between which there is nearly 20% difference. Two factors are inferred to result in the difference: 1) the amounts of DEHP sorption sites determined by specific surface areas in a mesoscopic view; 2) the intermolecular forces between DEHP molecules and

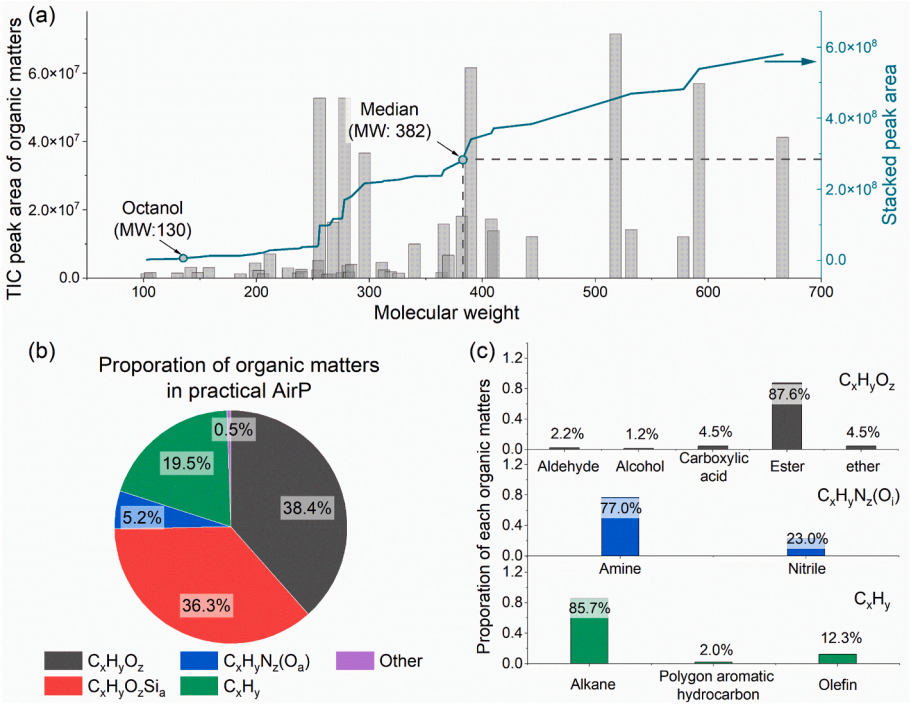

Fig. 5. (a) The tendency of organic-matter signals verified along molecular weight on realistic indoor airborne particles. (b) The organic-matter proportions of each content in realistic indoor airborne particles. (c) The classes of the organic-matter components in realistic indoor airborne particles for $C_xH_yO_z$, $C_xH_yN_z(O_i)$ and C_xH_y.

inorganic components in a microscopic view.

The variations of the differential specific surface area over pore diameter can be seen in Figs. S7a and b for ATD and BJD, respectively. Micro-pores in both ATD and BJD ranged from 1 nm to 10 nm in diameter. The median diameters of micro-pores are similar for ATD and BJD, the values of which were 3.8 nm and 3.1 nm, respectively. The specific areas can be calculated by accumulating the specific pore areas, and the values are 24.2 m^2/g and 18.6 m^2/g for ATD and BJD, respectively. Thus, ATD had a more than 20% larger surface area than BJD under the same mass. It means that ATD could provide extra 20% sorption sites for DEHP molecules than BJD and then obtain a larger DEHP adsorption capacity.

The elemental compositions were characterized as nearly the same for ATD and BJD as shown in Fig. S8a, indicating the similar intermolecular forces between DEHP molecules and the two dust. Silicon, aluminum, iron and calcium occupy the top four in contents for both ATD and BJD, the values of which are 24.8%, 3.91%, 2.93%, 2.29% for ATD and 27.7%, 4.76%, 2.34%, 4.77% for BJD, respectively. The rest elements are hardly contained in ATD and BJD, with nearly or less than 1% in content. Among all the detected elements, iron (Fe) is the one that should be concerned for its potential coordination ability on molecules with electron pairs [46,47]. Figs. S8b and c revealed the Fe oxidation states and contents in ATD and BJD, respectively. There are split peaks for Fe spectrums displayed at 726.35 eV and 712.00 eV for ATD and 726.85 eV and 711.80 eV for BJD, respectively. It means the energy of the valence electron level varied, mainly depending on the oxidation states of Fe elements [48–50]. The Fe^{2+} and Fe^{3+} occupied 23.0%, 77.0% in ATD and 25.0%, 75.0% in BJD, respectively, through fitting the bands. Thus, the Fe element composition was similar in ATD and BJD, resulting in the same coordination capacity of Fe ions for DEHP molecules.

4.3. Organic film formation on AirP and BJD

According to our previous studies, the DEHP sorption states were characterized in the organic-film phase on indoor impermeable surfaces [18], and the films could then form the combined pollution through enriching indoor VOCs to be more hazardous [19]. Thus, we further characterized the DEHP film formations on AirP and BJD by atomic force microscope (AFM) in this study. The method of organic film detection was described in detail in *Section S8* of the Supplementary Material. The box charts of adhesion forces varying over time are shown in Fig. 6a and b. There were large increases in adhesion forces for AirP and BJD after the first 8-day DEHP exposure, the median of which varied from 4.0 nN to 11.9 nN for AirP and from 3.6 nN to 10.1 nN for BJD, respectively. Then, the adhesion forces stayed nearly invariable during the latter 10 days' exposure. The increasing adhesion forces indicated that the DEHP organic films were formed on both AirP and BJD surfaces. Based on the measured K_{ap} and K_{dust} above, we simulated the DEHP sorption process on silicon-slice based AirP and BJD with the model listed in eq. (S9) of the Supplementary Material. The surface DEHP concentrations on the particle samples and silicon slices were then calculated, as shown in Fig. 6a and b. The AirP samples reached sorption balance after nearly 8–10 days' exposure. As a comparison, only 2–3 days were spent for BJD samples to reach a steady state of DEHP sorption. It should be noted that the DEHP amounts enriched on AirP were several orders of magnitude larger than those on BJD, while the differences in adhesion forces were only 1.8 nN (no more than 18%). The phenomenon indicates that DEHP organic films have been fully covered on the AirP and BJD particle surfaces, and then the AFM probe detected similar adhesion forces when touching the samples. Due to the inherent organic matters, AirP was supposed to have a larger film thickness on the particle surface, leading to relatively larger adhesion forces than BJD.

The organic films were distributed heterogeneously on AirP and BJD surfaces, as shown in Fig. 6c and d. When the probe scanned the AirP and BJD (see the circle-highlighted roughness graphs in Fig. 6c and d), the surface topography continuously increased and was shown as peaks. In contrast, the adhesion forces were detected to increase slightly when the probe first touched the particles, which, however, decreased acutely as the topography elevated. The phenomenon was also clearly described

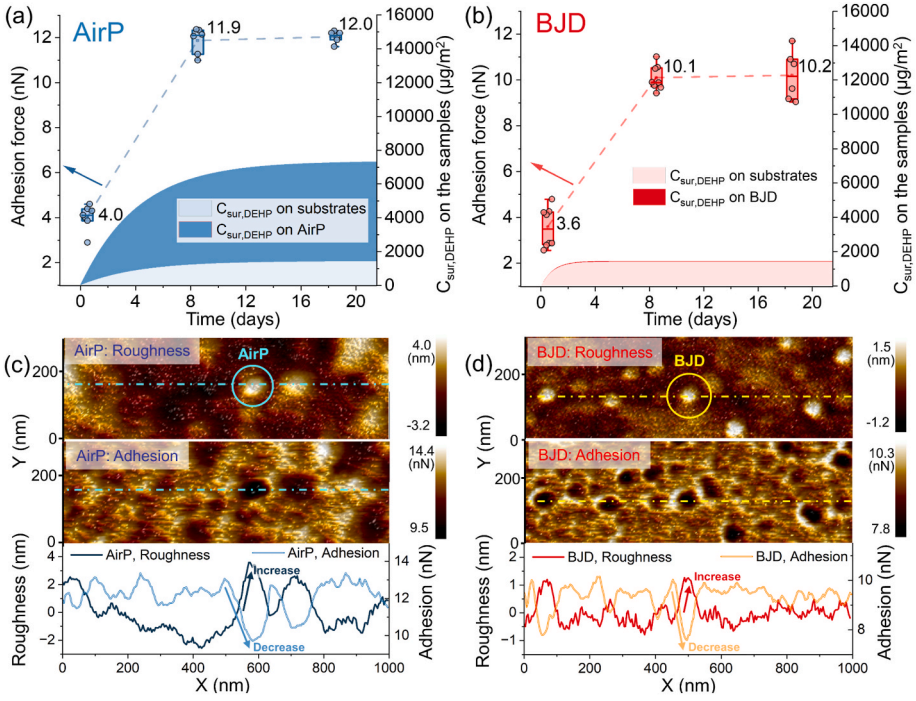

Fig. 6. The variations of adhesion forces and the calculated surface DEHP concentrations on (a) AirP and (b) BJD samples. The surface topographies and adhesions of DEHP on (c) AirP and (d) BJD samples to characterize the organic film distribution, in which the figures containing roughness, adhesion and data plots of AirP and BJD are stacked. The dish-point lines in (c) and (d) mean the samplings on roughness and adhesion, the results of which can be seen in the data plots below. The circles in roughness graphs highlight the AirP and BJD, the roughness and adhesion variations of which were marked by arrows in data plots.

through the marked arrows in the data plots of Fig. 6c and d. It means that there were more DEHP organic films accumulated on the bottom of particles when the AirP and BJD were loaded on plat surfaces. With the knowledge of DEHP organic film formation, the airborne particles and settled dust can potentially enrich other organic pollutants and then form more hazardous combined pollution.

4.4. Implications for further work

This study can support further valuable work. Firstly, it is worth quantifying the DEHP partitioning capacity on realistic indoor settled dust, which was not explored in this study due to a shortage of indoor dust collecting methods. A vacuum cleaner-based dust-collecting method was developed in Bi's study [13], which is expected to be conducted in the future. According to the dust characterization, the organic matter fraction of indoor dust was approximated as 0.2, similar to airborne particles [10]. Therefore, the K_{dust} of realistic indoor dust is inferred to be in the same order of magnitude as K_{ap} determined in this study. Secondly, it is worth quantifying the capacity of DEHP organic films on particles to enrich other indoor pollutants. Previous research has proven that human exposure to DEHP mainly occurs through airborne-particle inhalation and dust ingestion by metabolism analysis [3], field tests [7,8] and modeling analysis [2]. Thus, it is urgent to determine the capacity of DEHP film on particles to enrich other indoor pollutants and form more hazardous combined pollution. We have experimentally discovered that the film-phase DEHP on an indoor surface could observably capture indoor VOCs with a hydroxyl group in molecular structures in a previous study [19]. A similar phenomenon is expected to be observed for the organic films on the airborne particles and settled dust.

Some limitations also remain to be refined in the future. The humidity level was controlled at 50% by pretreated clean air for a jar-like chamber instead of the natural indoor air. The pretreated air can prevent the chamber from being polluted but may also introduce errors in DEHP-partition-coefficient determination because of the controlled humidity. Zhou et al. have experimentally proved that humidity had a negligible effect on partition-coefficient determination, and no apparent law was found [31]. The effect of humidity on DEHP sorption remains to be further studied. Meanwhile, the mass transfer coefficients, h_m, controlled by the air velocities, had discrepancies with the real indoor environments. As it was discussed in Sections 3.2 and *3.3*, the h_m of DEHP were held as 730.7 m/h and 36.9 m/h for airborne particles and road dust, respectively. According to the reported data, h_m values were determined as 7.82×10^2 - 1.19×10^4 m/h for airborne particles [35,38] and 0.106–1.63 m/h for settled dust [11,12] in real indoor environments. In this study, the h_m of airborne particles was smaller, and that of settled dust was larger than in real environmental conditions. According to the heat and mass transfer theory, the h_m parameter mainly affected the time reaching sorption balance instead of DEHP sorption amounts. Thus, the differences in air velocity and h_m value between this study and real indoor environments were expected to have little influence on the partition-coefficient determination. The deductions are required to be verified by further experiments.

5. Conclusions

This study presented a direct particle sorption method to measure the DEHP partition coefficients of realistic airborne particles (AirP), as well as Arizona test dust (ATD) and Beijing road dust (BJD) samples. We developed mechanistic models that describe the DEHP sorption processes from air to particles in chambers to determine the DEHP partition coefficients. The DEHP partition coefficient of AirP (K_{ap}) was characterized as 4.03×10^4 m^3/g, while those of ATD and BJD (K_{dust}) were 433 m^3/g and 366 m^3/g, respectively. We systematically discussed the key factors that dominate DEHP sorption capacities on different particles. The key factors included organic carbon proportion, particle specific area and inorganic elemental components. Since AirP comprised 33.0% organic carbons, it exhibited a DEHP absorbing behavior in AirP, leading to a significantly larger DEHP partition capacity compared to the inorganic ATD and BJD. Furthermore, we identified the relatively larger specific surface area as the key factor resulting in a larger K_{dust} of ATD than BJD. In contrast, no apparent effect on DEHP sorption behavior was found caused by inorganic elemental components since ATD is similar to BJD in elemental composition. Further research is necessary to investigate the impact of environmental conditions, such as temperature and humidity, on the DEHP partition coefficients.

This study revealed three orders of magnitude deviations in the reported K_{ap} from the literature, which could be attributed to errors introduced by empirical formulas and particle compositions. DEHP organic films forming on AirP and BJD are also characterized during the sorption experiments, which had the potential to form more hazardous combined pollution when exposed to other indoor pollutants. Overall, the direct particle sorption method and more accurate partition coefficients obtained in this study provide a valuable scientific basis for correctly evaluating the DEHP concentrations in airborne particles and settled dust in indoor environments.

CRediT authorship contribution statement

Zhuo Chen: Writing – review & editing, Writing – original draft, Resources, Methodology, Investigation, Formal analysis, Data curation. **Fanxuan Xia:** Writing – review & editing, Visualization, Resources. **Yujie Fan:** Writing – review & editing, Visualization, Resources. **Yi Jiang:** Writing – review & editing, Supervision, Conceptualization. **Ying Xu:** Supervision, Conceptualization. **Jinhan Mo:** Writing – review & editing, Supervision, Methodology, Funding acquisition, Conceptualization.

Declaration of competing interest

The authors declare that they have no known competing financial interests or personal relationships that could have appeared to influence the work reported in this paper.

Data availability

Data will be made available on request.

Acknowledgments

The research was supported by the National Key Research and Development Program of China (No. 2022YFC3702803) and the National Natural Science Foundation of China (No. 52325801, 52078269).

Appendix A. Supplementary data

Supplementary data to this article can be found online at https://doi.org/10.1016/j.buildenv.2024.111273.

References

[1] Y. Cao, L. Li, K.H. Shen, J.G. Liu, Disease burden attributable to endocrine-disrupting chemicals exposure in China: a case study of phthalates, Sci. Total Environ. 662 (2019) 615–621, https://doi.org/10.1016/j.scitotenv.2019.01.255.
[2] J.C. Little, C.J. Weschler, W.W. Nazaroff, Z. Liu, E.A.C. Hubal, Rapid methods to estimate potential exposure to semivolatile organic compounds in the indoor environment, Environ. Sci. Technol. 46 (20) (2012) 11171–11178, https://doi.org/10.1021/es301088a.
[3] G. Beko, C.J. Weschler, S. Langer, M. Callesen, J. Toftum, G. Clausen, Children's phthalate intakes and resultant cumulative exposures estimated from urine compared with estimates from dust ingestion, inhalation and dermal absorption in their homes and daycare centers, PLoS One 8 (4) (2013), https://doi.org/10.1371/journal.pone.0062442.
[4] H. Fromme, T. Lahrz, M. Piloty, H. Gebhart, A. Oddoy, H. Ruden, Occurrence of phthalates and musk fragrances in indoor air and dust from apartments and

kindergartens in Berlin (Germany), Indoor Air 14 (3) (2004) 188–195, https://doi.org/10.1046/j.1600-0668.2003.00223.x.
[5] Q. Chen, E. Tian, Z. Luo, J. Mo, Adsorption film with sub-milli-interface morphologies via direct ink writing for indoor formaldehyde removal, J. Hazard Mater. 427 (2022) 128190, https://doi.org/10.1016/j.jhazmat.2021.128190.
[6] Q. Chen, E. Tian, Y. Wang, J. Mo, G. Xu, M. Zhu, Recent Progress and perspectives of direct ink writing applications for mass transfer enhancement in gas-phase adsorption and catalysis, Small Methods 7 (6) (2023) 2201302, https://doi.org/10.1002/smtd.202201302.
[7] X. Wang, W. Tao, Y. Xu, J. Feng, F. Wang, Indoor phthalate concentration and exposure in residential and office buildings in Xi'an, China, Atmos. Environ. 87 (2014) 146–152, https://doi.org/10.1016/j.atmosenv.2014.01.018.
[8] Z.M. Bu, Y.P. Zhang, D. Mmereki, W. Yu, B.Z. Li, Indoor phthalate concentration in residential apartments in Chongqing, China: implications for preschool children's exposure and risk assessment, Atmos. Environ. 127 (2016) 34–45, https://doi.org/10.1016/j.atmosenv.2015.12.010.
[9] C.J. Weschler, W.W. Nazaroff, Semivolatile organic compounds in indoor environments, Atmos. Environ. 42 (40) (2008) 9018–9040, https://doi.org/10.1016/j.atmosenv.2008.09.052.
[10] C.J. Weschler, W.W. Nazaroff, SVOC partitioning between the gas phase and settled dust indoors, Atmos. Environ. 44 (30) (2010) 3609–3620, https://doi.org/10.1016/j.atmosenv.2010.06.029.
[11] S. Shi, B. Zhao, Modeled exposure assessment via inhalation and dermal pathways to airborne semivolatile organic compounds (SVOCs) in residences, Environ. Sci. Technol. 48 (10) (2014) 5691–5699, https://doi.org/10.1021/es500235q.
[12] C.Y. Bi, Y.R. Liang, Y. Xu, Fate and transport of phthalates in indoor environments and the influence of temperature: a case study in a test house, Environ. Sci. Technol. 49 (16) (2015) 9674–9681, https://doi.org/10.1021/acs.est.5b02787.
[13] C. Bi, X. Wang, H. Li, X. Li, Y. Xu, Direct transfer of phthalate and alternative plasticizers from indoor source products to dust: laboratory measurements and predictive modeling, Environ. Sci. Technol. 55 (1) (2021) 341–351, https://doi.org/10.1021/acs.est.0c05131.
[14] C. Liu, B. Zhao, Y. Zhang, The influence of aerosol dynamics on indoor exposure to airborne DEHP, Atmos. Environ. 44 (16) (2010) 1952–1959, https://doi.org/10.1016/j.atmosenv.2010.03.002.
[15] W. Wei, C. Mandin, O. Blanchard, F. Mercier, M. Pelletier, B. Le Bot, P. Glorennec, O. Ramalho, Distributions of the particle/gas and dust/gas partition coefficients for seventy-two semi-volatile organic compounds in indoor environment, Chemosphere 153 (2016) 212–219, https://doi.org/10.1016/j.chemosphere.2016.03.007.
[16] Y.R. Liang, Y. Xu, Improved method for measuring and characterizing phthalate emissions from building materials and its application to exposure assessment, Environ. Sci. Technol. 48 (8) (2014) 4475–4484, https://doi.org/10.1021/es405809r.
[17] Y.X. Wu, C.M.A. Eichler, W.N. Leng, S.S. Cox, L.C. Marr, J.C. Little, Adsorption of phthalates on impervious indoor surfaces, Environ. Sci. Technol. 51 (5) (2017) 2907–2913, https://doi.org/10.1021/acs.est.6b05853.
[18] Z. Chen, Q.Y. Wu, Y. Xu, J.H. Mo, Partitioning of airborne PAEs on indoor impermeable surfaces: a microscopic view of the sorption process, J. Hazard Mater. 424 (2022), https://doi.org/10.1016/j.jhazmat.2021.127326.
[19] Z. Chen, Q. Chen, Y. Xu, J. Mo, Partitioning characteristics of indoor VOCs on impermeable surfaces covered by film-phase DnBP and DEHP, J. Hazard. Mater. Adv. 8 (2022) 100191, https://doi.org/10.1016/j.hazadv.2022.100191.
[20] Z. Sun, C. Liu, Y. Zhang, Evaluation of a steady-state method to estimate indoor PM2.5 concentration of outdoor origin, Build. Environ. 161 (2019) 106243 j.buildenv.2019.106243.
[21] E. Tian, Y. Gao, J. Mo, Experimental studies on electrostatic-force strengthened particulate matter filtration for built environments: progress and perspectives, Build. Environ. 228 (2023) 109782, https://doi.org/10.1016/j.buildenv.2022.109782.
[22] X.Q. Pei, M. Song, M. Guo, F.F. Mo, X.Y. Shen, Concentration and risk assessment of phthalates present in indoor air from newly decorated apartments, Atmos. Environ. 68 (2013) 17–23, https://doi.org/10.1016/j.atmosenv.2012.11.039.
[23] F. Alliot, E. Moreau-Guigon, C. Bourges, A. Desportes, M.J. Teil, M. Blanchard, M. Chevreuil, A multi-residue method for characterization of endocrine disruptors in gaseous and particulate phases of ambient air, Atmos. Environ. 92 (2014) 1–8, https://doi.org/10.1016/j.atmosenv.2014.02.044.
[24] X.Z. Ouyang, M. Xia, X.Y. Shen, Y. Zhan, Pollution characteristics of 15 gas- and particle-phase phthalates in indoor and outdoor air in Hangzhou, J. Environ. Sci. 86 (2019) 107–119, https://doi.org/10.1016/j.jes.2019.05.008.
[25] L. Huang, Y. Qiao, S. Deng, M. Zhou, W. Zhao, Y. Yue, Airborne phthalates in indoor environment: partition state and influential built environmental conditions, Chemosphere 254 (2020) 126782, https://doi.org/10.1016/j.chemosphere.2020.126782.
[26] M. Song, C.C. Chi, M. Guo, X.Q. Wang, L.X. Cheng, X.Y. Shen, Pollution levels and characteristics of phthalate esters in indoor air of offices, J. Environ. Sci. 28 (2015) 157–162, https://doi.org/10.1016/j.jes.2014.05.051.
[27] S.S. Wang, J.L. Nan, C.Z. Shi, Q.Y. Fu, S. Gao, D.F. Wang, H.X. Cui, A. Saiz-Lopez, B. Zhou, Atmospheric ammonia and its impacts on regional air quality over the megacity of Shanghai, China, Sci. Rep. 5 (2015), https://doi.org/10.1038/srep15842.
[28] C.C. Chi, M. Xia, C. Zhou, X.Q. Wang, M.L. Weng, X.Y. Shen, Determination of 15 phthalate esters in air by gas-phase and particle-phase simultaneous sampling, J. Environ. Sci. 55 (2017) 137–145, https://doi.org/10.1016/j.jes.2016.01.036.
[29] J.L. Benning, Z. Liu, A. Tiwari, J.C. Little, L.C. Marr, Characterizing gas-particle interactions of phthalate plasticizer emitted from vinyl flooring, Environ. Sci. Technol. 47 (6) (2013) 2696–2703, https://doi.org/10.1021/es304725b.
[30] Y.X. Wu, C.M.A. Eichler, J.P. Cao, J. Benning, A. Olson, S.Y. Chen, C. Liu, E. P. Vejerano, L.C. Marr, J.C. Little, Particle/gas partitioning of phthalates to organic and inorganic airborne particles in the indoor environment, Environ. Sci. Technol. 52 (6) (2018) 3583–3590, https://doi.org/10.1021/acs.est.7b05982.
[31] X.J. Zhou, J.L. Lian, Y. Cheng, X.K. Wang, The gas/particle partitioning behavior of phthalate esters in indoor environment: effects of temperature and humidity, Environ. Res. 194 (2021), https://doi.org/10.1016/j.envres.2020.110681.
[32] A. Li, C. Liu, L.Y. Kang, K. Liu, X.K. Wang, Chamber study on the migration of di-n-octyl phthalate (DNOP) between source surfaces and settled dust: influence of temperature and dust loading, Atmos. Environ. 268 (2022), https://doi.org/10.1016/j.atmosenv.2021.118789.
[33] S. Jeon, K.-T. Kim, K. Choi, Migration of DEHP and DINP into dust from PVC flooring products at different surface temperature, Sci. Total Environ. 547 (2016) 441–446, https://doi.org/10.1016/j.scitotenv.2015.12.135.
[34] Y. Xu, J.C. Little, Predicting emissions of SVOCs from polymeric materials and their interaction with airborne particles, Environ. Sci. Technol. 40 (2) (2006) 456–461, https://doi.org/10.1021/es051517j.
[35] Y.R. Liang, C.Y. Bi, X.K. Wang, Y. Xu, A general mechanistic model for predicting the fate and transport of phthalates in indoor environments, Indoor Air 29 (1) (2019) 55–69, https://doi.org/10.1111/ina.12514.
[36] R.J. Li, L.Y. Kang, S.J. Wu, X.J. Zhou, X.K. Wang, Effect of dust formation on the fate of indoor phthalates: model analysis, Build. Environ. 229 (2023), https://doi.org/10.1016/j.buildenv.2022.109957.
[37] J.P. Cao, C.J. Weschler, J.J. Luo, Y.P. Zhang, Cm-history method, a novel approach to simultaneously measure source and sink parameters important for estimating indoor exposures to phthalates, Environ. Sci. Technol. 50 (2) (2016) 825–834, https://doi.org/10.1021/acs.est.5b04404.
[38] W. Li, E.J. Davis, Aerosol evaporation in the transition regime, Aerosol. Sci. Technol. 25 (1) (1996) 11–21, https://doi.org/10.1080/02786829608965375.
[39] C. Liu, S.S. Shi, C. Weschler, B. Zhao, Y.P. Zhang, Analysis of the dynamic interaction between SVOCs and airborne particles, Aerosol. Sci. Technol. 47 (2) (2013) 125–136, https://doi.org/10.1080/02786826.2012.730163.
[40] J.F. Pankow, An absorption model of gas/particle partitioning of organic compounds in the atmosphere, Atmos. Environ. 28 (2) (1994) 185–188, https://doi.org/10.1016/1352-2310(94)90093-0.
[41] C. Liu, G.C. Morrison, Y. Zhang, Role of aerosols in enhancing SVOC flux between air and indoor surfaces and its influence on exposure, Atmos. Environ. 55 (2012) 347–356, https://doi.org/10.1016/j.atmosenv.2012.03.030.
[42] S. Shi, B. Zhao, Estimating indoor semi-volatile organic compounds (SVOCs) associated with settled dust by an integrated kinetic model accounting for aerosol dynamics, Atmos. Environ. 107 (2015) 52–61, https://doi.org/10.1016/j.atmosenv.2015.01.076.
[43] L. Kang, S. Wu, K. Liu, X. Wang, X. Zhou, Direct and non-direct transfer of phthalate esters from indoor sources to settled dust: model analysis, Build. Environ. 202 (2021) 108012, https://doi.org/10.1016/j.buildenv.2021.108012.
[44] Y.F. Li, W.L. Ma, M. Yang, Prediction of gas/particle partitioning of polybrominated diphenyl ethers (PBDEs) in global air: a theoretical study, Atmos. Chem. Phys. 15 (4) (2015) 1669–1681, https://doi.org/10.5194/acp-15-1669-2015.
[45] H.L. Li, P.F. Yang, L.Y. Liu, B.B. Gong, Z.F. Zhang, W.L. Ma, R.W. Macdonald, A. N. Nikolaev, Y.F. Li, Steady-state based model of airborne particle/gas and settled dust/gas partitioning for semivolatile organic compounds in the indoor environment, Environ. Sci. Technol. 56 (12) (2022) 8373–8383, https://doi.org/10.1021/acs.est.1c07819.
[46] K.M. Vogel, P.M. Kozlowski, M.Z. Zgierski, T.G. Spiro, Determinants of the FeXO (X = C, N, O) vibrational frequencies in heme adducts from experiment and density functional theory, J. Am. Chem. Soc. 121 (43) (1999) 9915–9921, https://doi.org/10.1021/ja990042r.
[47] Y. Man, Z.M. Li, W.L. Kong, W.H. Li, W.W. Dong, Y.Q. Wang, F.Z. Xie, D.L. Zhao, Q. S. Qu, W.S. Zou, Starch fermentation wastewater as a precursor to prepare S,N-doped carbon dots for selective Fe(III) detection and carbon microspheres for solution decolorization, Microchem. J. 159 (2020), https://doi.org/10.1016/j.microc.2020.105338.
[48] D. Hou, H. Tao, X. Zhu, M. Li, Polydopamine and MnO2 core-shell composites for high-performance supercapacitors, Appl. Surf. Sci. 419 (2017) 580–585, https://doi.org/10.1016/j.apsusc.2017.05.080.
[49] P.S. Bagus, C.J. Nelin, C.R. Brundle, B.V. Crist, N. Lahiri, K.M. Rosso, Combined multiplet theory and experiment for the Fe 2p and 3p XPS of FeO and Fe2O3, J. Chem. Phys. 154 (9) (2021), https://doi.org/10.1063/5.0039765.
[50] Y. Gao, E. Tian, J. Mo, Electrostatic Polydopamine-Interface-Mediated (e-PIM) filters with tuned surface topography and electrical properties for efficient particle capture and ozone removal, J. Hazard Mater. 441 (2023) 129821, https://doi.org/10.1016/j.jhazmat.2022.129821.